


Phase diagrams of the antiferromagnetic XY model on a triangular lattice with higher-order interactions

M. Lach  and M. Žukovič 

Department of Theoretical Physics and Astrophysics, Institute of Physics, Faculty of Science, Pavol Jozef Šafárik University in Košice, Park Angelinum 9, 041 54 Košice, Slovak Republic

 (Received 5 May 2021; revised 6 August 2021; accepted 9 August 2021; published 26 August 2021)

We study the effects of higher-order antinematic interactions on the critical behavior of the antiferromagnetic (AFM) XY model on a triangular lattice using Monte Carlo simulations. The parameter q of the generalized antinematic (ANq) interaction is found to have a pronounced effect on the phase diagram topology by inducing new quasi-long-range ordered phases due to competition with the conventional AFM interaction as well as geometrical frustration. For values of q divisible by 3, the ground-state competition between the two interactions results in a frustrated canted AFM phase appearing at low temperatures wedged between the AFM and ANq phases. For q nondivisible by 3, with the increase of q one can observe the evolution of the phase diagram topology featuring two ($q = 2$), three ($q = 4, 5$), and four ($q \geq 7$) ordered phases. In addition to the two phases previously found for $q = 2$, the first new phase with solely AFM ordering arises for $q = 4$ in the limit of strong AFM coupling and higher temperatures by separating from the phase with the coexisting AFM and ANq orderings. For $q = 7$, another phase with AFM ordering but multimodal spin distribution in each sublattice appears at intermediate temperatures. All these algebraic phases also display standard and generalized chiral long-range orderings, which decouple at higher temperatures in the regime of dominant ANq (AFM) interaction for $q \geq 4$ ($q \geq 7$) preserving only the generalized (standard) chiral ordering.

DOI: [10.1103/PhysRevE.104.024134](https://doi.org/10.1103/PhysRevE.104.024134)

I. INTRODUCTION

Although the two-dimensional XY model with short-range interactions and continuous symmetry lacks any form of true long-range ordering (LRO) [1], it still can undergo the Berezinskii-Kosterlitz-Thouless (BKT) phase transition [2,3]. The low-temperature phase remains critical for all temperatures below the transition point at T_{BKT} , displaying quasi-long-range ordering (QLRO) with an algebraically decaying spin-spin correlation function due to bound pairs of vortices and antivortices. At T_{BKT} , the infinite-order phase transition leads to unbinding of the vortex-antivortex pairs and a completely disordered phase with an exponentially decaying correlation function. The behavior of the standard XY model is well understood; nevertheless, its many generalizations remain an active subject of study due to rich and interesting critical behavior [4–23], in connection with experimental realizations [11,24–27] and the potential for interdisciplinary applications [28–32].

Most of the above generalizations of the standard XY model are based on inclusion of higher-order interactions. Namely, besides the usual magnetic interaction with spin angle periodicity of 2π , there is an additional (generalized) nematic interaction characterized by a positive integer q such that its periodicity is $2\pi/q$. Such a term produces vortices with noninteger $1/q$ winding number, which compete with the conventional vortices and antivortices generated by the

magnetic interaction. The Hamiltonian of such a generalized model can be expressed in the form

$$\mathcal{H} = -J_1 \sum_{\langle i,j \rangle} \cos(\phi_{i,j}) - J_q \sum_{\langle i,j \rangle} \cos(q\phi_{i,j}), \quad (1)$$

where the summations run over the nearest-neighbor spins, $\phi_{i,j} = \phi_i - \phi_j$ is the angle between two neighboring spins at sites i and j , and J_1 and J_q are the exchange interaction parameters. The first term J_1 is a usual magnetic, i.e., FM ($J_1 > 0$) or AFM ($J_1 < 0$) coupling, while the second term J_q represents a generalized nematic, Nq ($J_q > 0$) or ANq ($J_q < 0$) interaction.

When $q = 2$ and both J_1 and J_2 are positive, the inclusion of the nematic N2 term leads to the appearance of the FM and the nematic N2 QLRO phases, with the phase transition belonging to the Ising universality class [5–8,12,13,33]. Additionally, theoretical investigations of the model with the competing FM ($J_1 > 0$) and AN2 ($J_2 < 0$) interactions revealed the existence of a new canted ferromagnetic phase at very low temperatures wedged between the FM and AN2 phases [16,22]. A recent series of papers [17–19] studied the effect of the gradual increase of the parameter $q > 2$ on the critical properties of the model with both J_1 and J_q positive. It was found that the higher-order interactions lead to a qualitatively different phase diagrams from the one observed for $q = 2$. In particular, for $q \geq 4$ they revealed up to two additional ordered phases originating from the competition between the FM and Nq couplings, with the phase transitions belonging to a variety of universality classes.

*milan.zukovic@upjs.sk

The above studies assumed a bipartite (square) lattice, on which the character of the magnetic interaction (the sign of J_1) is not expected to change the phase diagram. However, in the model on a nonbipartite (e.g., triangular) lattice, the AFM ($J_1 < 0$) interaction leads to geometrical frustration, which can drastically change the critical behavior. Such a model has been intensively studied [34–39] due to the possibility of spin-chirality decoupling, where the transitions to the magnetic QLRO and the vector chiral LRO phases occur at different temperatures. The inclusion of the AN2 ($J_2 < 0$) term leads to the emergence of the AFM and AN2 phases, with the transition belonging to the Ising universality class [14]. Thus, the phase diagram topology as well as the character of the phase transition between the ordered phases are similar to those of the FM-N2 case. Nevertheless, the AFM-AN2 model additionally displays a chiral LRO that slightly extends above the BKT line.

In our recent study of the geometrically frustrated AFM-AN q model on a triangular lattice [23], we demonstrated that the nematic parameter increased to $q = 3$ induces a new peculiar canted antiferromagnetic (CAFM) phase. It appears at low temperatures, situated between the AFM and AN3 phases, with the AFM-CAFM and AN3-CAFM phase transitions belonging to the weak Ising and weak three-state Potts universality classes, respectively. Thus, compared to the non-frustrated FM-N q model in which the increasing $q > 2$ first changed the phase diagram topology for $q = 4$ [19], in the frustrated AFM-AN q case such a change occurred already for $q = 3$. Apparently, the effect of the increasing q in the two cases is different, and thus we find it interesting to study the evolution of the phase diagram topology with the increasing order of the generalized nematic coupling also in the latter case. The groundwork for such a study has already been laid in our previous work [31], which focused on the ground states of this model for up to $q = 8$. In the present paper, we extend the investigation to finite temperatures with the goal to establish phase diagrams of the AFM-AN q models on the triangular lattice for $4 \leq q \leq 15$.

II. SIMULATIONS

We perform Monte Carlo (MC) simulations of the model (1) using the Metropolis algorithm. We consider the generalized nematic parameter $q = 4, 5, \dots, 10$ (with checks up to $q = 15$) and the interaction parameters J_1 and J_q in the form $J_1 = -\Delta$ and $J_q = \Delta - 1$, with $\Delta \in [0, 1]$ to cover the interactions between the pure AN q ($\Delta = 0$) and the pure AFM ($\Delta = 1$) limits. Periodic boundary conditions were used to simulate systems with a linear size L . Due to the highly efficient parallelized implementation on graphical processing units (GPUs), we were able to run extensive simulations of relatively large system sizes. For calculation of thermal averages of various quantities of interest, we typically use $L = 384$, and for studying spin distributions we consider much larger sizes up to $L = 1536$. We note that the selected values of L should be multiples of 3 to reflect the fact that the system consists of three interpenetrating sublattices and that the periodic boundary conditions are imposed. To obtain the thermal averages, at each temperature step 5×10^6 MC sweeps were performed, with 20% discarded for equilibration. The simulation at the

next temperature starts from the final configuration obtained at the previous temperature, which helps to keep the system near equilibrium throughout the whole simulation.

To detect phase transitions between various phases and to determine the respective phase diagrams, we calculate the following quantities: the internal energy per spin,

$$e = \frac{\langle \mathcal{H} \rangle}{L^2}, \quad (2)$$

the specific heat per spin,

$$c = \frac{\langle \mathcal{H}^2 \rangle - \langle \mathcal{H} \rangle^2}{T^2 L^2}, \quad (3)$$

the magnetic (m_1) and generalized nematic (m_2, m_3, \dots, m_q) QLRO parameters,

$$m_k = \frac{\langle M_k \rangle}{L^2} = \frac{1}{L^2} \left\langle \sqrt{3 \sum_{\alpha=1}^3 M_{k\alpha}^2} \right\rangle, \quad k = 1, 2, \dots, q; \\ \alpha = 1, 2, 3, \quad (4)$$

where $\mathbf{M}_{k\alpha}$ is the α th sublattice QLRO parameter vector given by

$$\mathbf{M}_{k\alpha} = \left(\sum_{i \in \alpha} \cos(k\phi_{\alpha i}), \sum_{i \in \alpha} \sin(k\phi_{\alpha i}) \right), \quad (5)$$

and finally the standard (κ_1) and generalized ($\kappa_2, \kappa_3, \dots, \kappa_q$) staggered chiralities,

$$\kappa_k = \frac{\langle K_k \rangle}{L^2} = \frac{1}{2L^2} \left\langle \left| \sum_{p^+ \in \Delta} \kappa_{kp^+} - \sum_{p^- \in \nabla} \kappa_{kp^-} \right| \right\rangle, \\ k = 1, 2, \dots, q, \quad (6)$$

where κ_{kp^+} and κ_{kp^-} are the local generalized chiralities for each elementary plaquette of upward and downward triangles, respectively, defined by

$$\kappa_{kp} = 2\{\sin[k(\phi_2 - \phi_1)] + \sin[k(\phi_3 - \phi_2)] \\ + \sin[k(\phi_1 - \phi_3)]\}/3\sqrt{3}. \quad (7)$$

The susceptibilities of the respective order parameters can be defined as

$$\chi_o = \frac{1}{TL^2} (\langle O^2 \rangle - \langle O \rangle^2), \\ O = M_1, M_2, \dots, M_q; K_1, K_2, \dots, K_q. \quad (8)$$

The above quantities are useful in identifying the character of the QLRO (from the order parameters) as well as a rough determination of the phase boundaries (from the response functions). We note that the focus of the present study is the evolution of the phase diagram topology in a wide parameter space rather than precise determination of the phase boundaries. The latter would involve a finite-size scaling (FSS) analysis, which would require tremendous computational demands even on GPU, and thus we leave such analysis for future considerations.

Nevertheless, in the cases when the above quantities do not provide conclusive evidence, we further perform a correlation analysis to more reliably determine different phases. Such

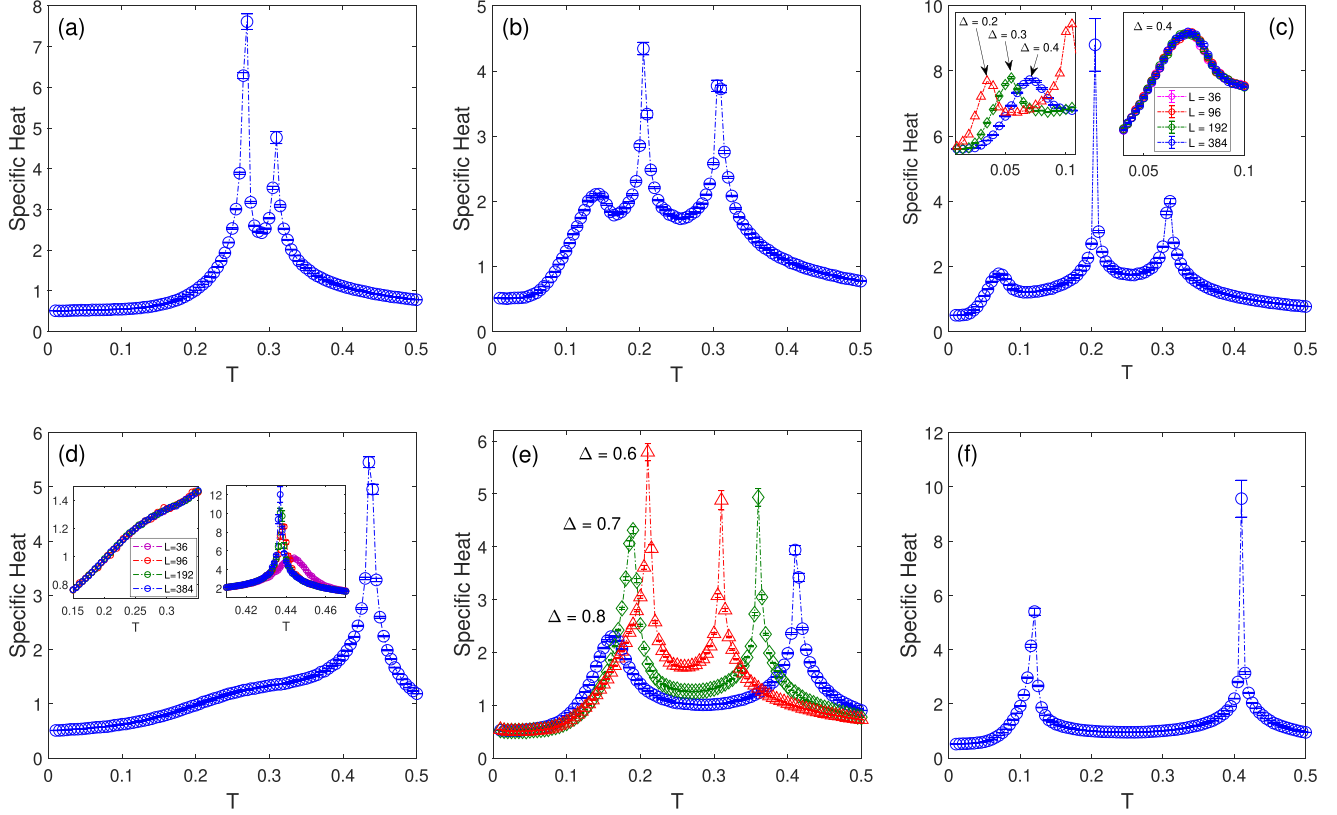


FIG. 1. Temperature dependencies of the specific heat c for $q = 4$ (left column) (a,d), $q = 7$ (middle column) (b,e), and $q = 10$ (right column) (c,f), corresponding to $\Delta = 0.4$ (upper row) (a,b,c) and $\Delta = 0.8$ (lower row) (d,e,f). In (c) and (e) the effect of Δ is demonstrated by adding curves for two more values. The second inset in (c) demonstrates finite-size effects at the low-temperature round peak, and the insets in (d) demonstrate finite-size effects at the low-temperature shoulder and high-temperature peak.

analysis is based on FSS of the QLRO parameters, obeying the scaling law

$$m_k(L) \propto L^{-\eta_{m_k}(T)}, \quad (9)$$

where $\eta_{m_k}(T)$ is the temperature-dependent critical exponent of the correlation function $G_k = \langle \cos(k\phi_{i,j}) \rangle$, $k = 1, \dots, q$. The transition temperature from the phase characterized by the parameter m_k can be determined as the temperature at which the critical exponent crosses to the value $\eta_{m_k} = 1$, characteristic for an exponential decay of the correlation function G_k .

III. RESULTS

The ground states of the present model were investigated in Ref. [31]. It was concluded that for q nondivisible by 3, the generalized nematic term prefers relative phase angles, which include $\Delta\phi = \pm 2\pi/3$, characteristic for the chiral AFM order observed in the standard XY model without higher-order couplings. Thus, there is no competition between the magnetic and generalized nematic interactions, and the system shows the chiral AFM ordering. However, for q divisible by 3, such sublattice-uniform ordering disappears. Instead, the neighboring spins belonging to different sublattices align, forming phase angles with the values dependent on the ratio of the exchange interactions J_1 and J_q in such a way that on each triangular plaquette two neighbors are oriented almost parallel

with respect to each other and almost antiparallel with respect to the third one. Such a microscopic arrangement results in a macroscopic degeneracy, loss of the sublattice uniformity, and the canted AFM (CAF) phase.

Our recent study of the model with $q = 3$ [23] showed that the CAF phase extends to finite temperatures and crosses to the AFM phase for dominant J_1 or to the AN3 phase for dominant J_3 or straight to the paramagnetic phase for J_1 and J_3 of comparable strengths. Thus, the increase of q from 2 to 3 resulted in the change of the phase diagram topology from the one with two phases (AFM and AN2) to that featuring three phases (AFM, AN3, and CAF). The results of the present study indicate that such a topology remains unchanged for any q divisible by 3 up to at least $q = 15$. Therefore, in the following, we will focus on the study of the phase diagram topology evolution with the increasing $q > 3$ for the values nondivisible by 3. As we will see, even though there is no competition between the AFM and AN q interactions for such cases in the ground state, there is still competition present at finite temperatures, which will result in the formation of new phases.

Potential phase transitions between different phases can be detected from the peaks in the response functions. In Fig. 1 we present temperature dependencies of the specific heat for $q = 4, 7$, and 10 in the regimes of the dominant AN q (for $\Delta = 0.4$ in the upper panels) and AFM (for $\Delta = 0.8$ in the lower panels) interactions. Focusing first on the case of $\Delta = 0.4$, for

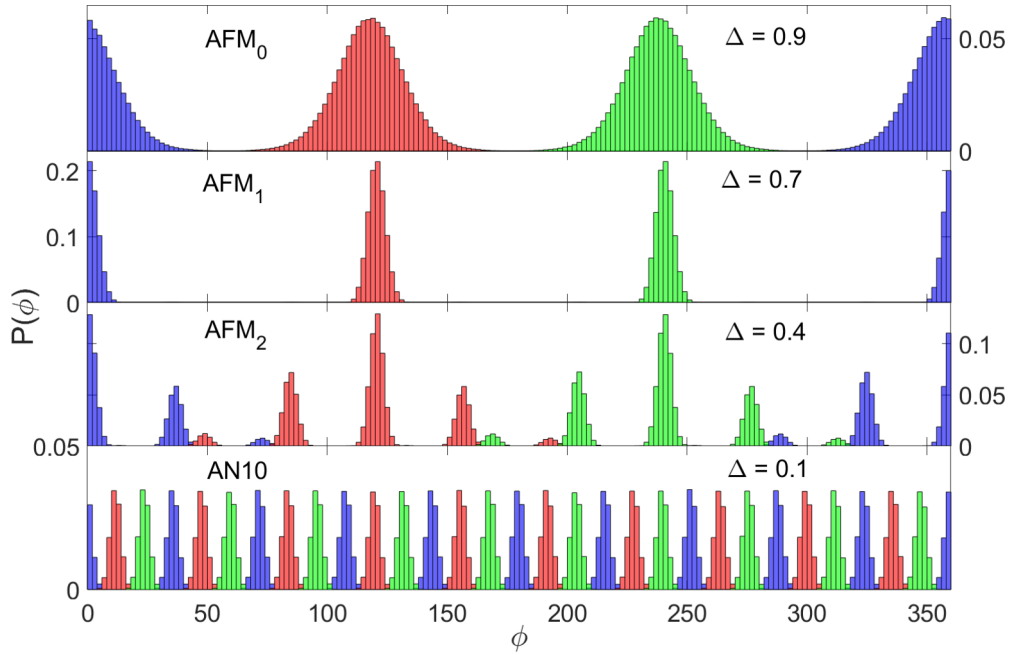


FIG. 2. Distributions of spin orientations in the observed phases for $q = 10$ at the fixed $T = 0.09$ and varying values of Δ , obtained from a single configuration snapshot with $L = 1536$. Different colors (shades) represent different sublattices.

$q = 4$ [Fig. 1(a)] one can observe two distinct sharp peaks, pointing to the presence of two phase transitions. However, for $q = 7$ [Fig. 1(b)] an additional rounder peak appears in the low-temperature region, and with the increasing q it shifts to lower temperatures [see Fig. 1(c) for $q = 10$]. The third peak may suggest the possibility of another phase transition and thus the existence of four different phases. Nevertheless, its insensitivity to the system size increase [see the top right inset of Fig. 1(c)] may correspond to a crossover rather than a genuine phase transition.

On the other hand, the picture is rather different in the regime when the AFM coupling prevails. The lower row in Fig. 1 shows that for $q = 4$ the specific heat displays only one sharp peak at higher temperatures and one relatively broad shoulder at lower temperatures [Fig. 1(d)]. The behavior of the respective anomalies with the increasing system size, shown in the insets, indicates their different characters. While with the increasing size the high-temperature peak becomes sharper, which is a typical behavior at a phase transition, the low-temperature shoulder is practically insensitive to the change of the system size. Nevertheless, with the increasing q , the broad shoulder evolves first to a round but distinct peak [see Fig. 1(e) for $q = 7$] and then to a sharp peak [see Fig. 1(f) for $q = 10$]. The low-temperature round peaks do not get sharper only with the increasing q but also with the decreasing Δ , as demonstrated in the top left inset of Fig. 1(c) and in Fig. 1(e). The question whether the round peaks reflect some kind of phase transition will be addressed below. Nevertheless, if all the anomalies observed in the specific-heat behavior signified different phase transitions, then we would witness the change of the phase diagram topology with the increasing q from the symmetric one with two phase transitions on each side of the interval Δ to the asymmetric one with three phase transitions for smaller and two phase transitions for larger Δ . Below we will try to shed more light on the critical behavior

associated with the presented anomalies in the specific heat and clarify the nature of the corresponding phases.

To understand the character of the spin ordering in the possible different phases, separated by the specific-heat anomalies, let us study spin distributions of microstates in the respective regions of the parameter space. Let us consider the case of $q = 10$, for which the observed anomalies appear the most pronounced. To capture the lowest-temperature phase in the three-phase-transitions scenario at smaller Δ and study its disappearance/transition into its counterpart in the two-phase-transitions structure at larger Δ , we fix the temperature to $T = 0.09$ and vary the value of Δ . In the lowest panel of Fig. 2 we present the distributions of spin orientations (angles) for $\Delta = 0.1$, i.e., in the limit of the strong AN q interaction. One can easily confirm that spins in each sublattice show $q = 10$ possible orientations distributed with equal weights and the spin angle periodicity of $2\pi/10$, as one would expect in the AN q phase. The appropriate order parameter (for finite systems) in this phase is thus m_{10} . With the increasing influence of the AFM coupling, the distribution undergoes a qualitative change, as demonstrated for $\Delta = 0.4$ in the second panel from the bottom. Spins in each sublattice display only five preferential orientations with different weights, which are confined to the same half-plane with the corresponding modes in different sublattices separated by the angle $2\pi/3$. Consequently, in each sublattice there is a net magnetization and the resulting AFM ordering between sublattices.

With further increase of the AFM coupling, the possible spin orientations become more constrained with a single preferential direction in each sublattice, as shown for $\Delta = 0.7$ in the second panel from the top. It is important to note that even though the resulting ordering is antiferromagnetic, it differs from the standard AFM phase in the absence of the higher-order coupling. In particular, due to the persisting

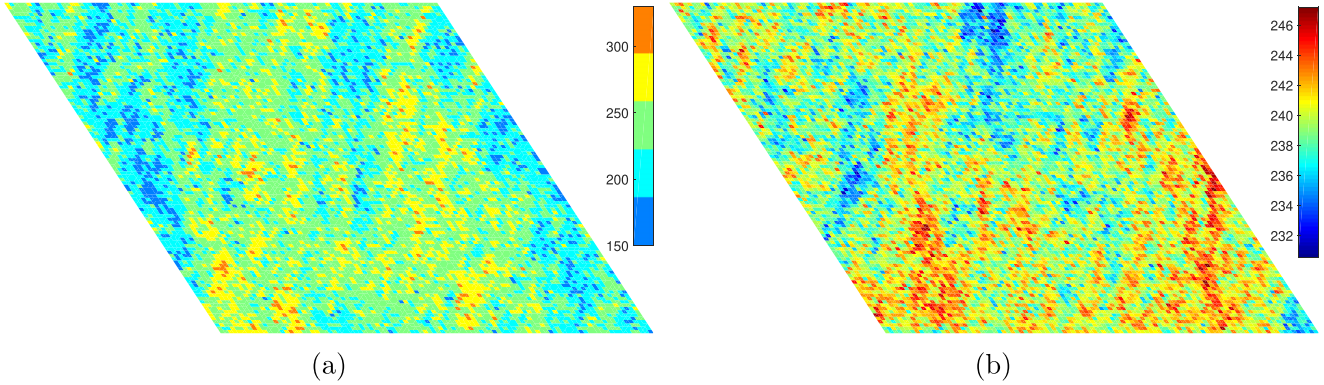


FIG. 3. Spin angle distributions in one of the three sublattices, corresponding to $q = 10$, $T = 0.09$ for (a) $\Delta = 0.4$ (left panel) and (b) $\Delta = 0.7$ (right panel).

effect of the ANq coupling, the widths of the sublattice spin distributions are constrained by the value $2\pi/q$. Considering the above arguments, the appropriate order parameter for the transition between these two peculiar AFM phases is m_5 . Finally, in the strong limit of the AFM coupling, such as that for $\Delta = 0.9$ presented in the top panel of Fig. 2, the ordering becomes usual AFM, for which the spin distribution widths are only controlled by the temperature, and the appropriate order parameter is m_1 . One can notice that in this phase the distributions become much wider than for $\Delta = 0.7$, even though the temperature remains the same.

The differences in the spin orderings at $\Delta = 0.4$ and 0.7 , which are both different from the usual AFM ordering at $\Delta = 0$, are illustrated in the snapshots presented in Fig. 3. For clarity, spin configurations (angles) are shown only in one of the three sublattices [the snapshots on the remaining sublattices look similar with shifted mean values, as shown by different colors (shades) in Fig. 2]. Notice the different scales in the two plots. While the spin angles for $\Delta = 0.4$ are distributed around five modes centered at $\phi = 4\pi/3$ with the frequencies corresponding to the green histogram in the second panel from the bottom of Fig. 2, those for $\Delta = 0.7$ have a unimodal distribution in a much narrower interval, in accordance with the green histogram in the second panel from the top.

In Fig. 4 we present the distributions of relative spin angles, $\Delta\phi = \phi_i - \phi_j$, between neighboring spins for the same parameters as in Fig. 2, which provide more information about local spin arrangements. In particular, one can clearly observe that the influence of even a relatively small ANq coupling (for $\Delta = 0.9$ in the upper panel) or AFM coupling (for $\Delta = 0.1$ in the bottom panel) can distort the symmetric distributions around $\Delta\phi = \pm 2\pi/3$ in the former case and reweigh and shift the equally weighted distributions around $\Delta\phi = \pm k\pi/q$, $k = 1, \dots, q$ in the latter case.

Having characterized various phases and defined the appropriate parameters for magnetic and nematic ordering, let us examine their behavior, as well as the behavior of the corresponding response functions, in order to establish the respective phase boundaries. In Fig. 5 we present temperature variations of the relevant generalized magnetic order parameters, and in Fig. 6 we present the corresponding susceptibilities, for $q = 4, 7$ and 10 , again in the

regimes of the superior ANq ($\Delta = 0.4$) and AFM ($\Delta = 0.8$) interactions.

For $\Delta = 0.4$ (upper rows in Figs. 5 and 6), the respective order parameters, as well as the corresponding susceptibilities, indeed indicate two ($q = 4$) and three ($q = 7$ and 10) phase transitions, signaled by the anomalies in the specific heat above. From the order parameters it follows that for $q = 4$ the system first displays the phase transition from the paramagnetic (P) to the AN4 phase, followed by another transition to the AFM phase at lower temperatures. The low-temperature phase thus features both the AN4 and AFM orderings. To distinguish it from the standard AFM₀ phase with no AN4 ordering, observed in the limit of large Δ , we will refer to it as the AFM₁ phase. For $q = 7$ and 10 , another phase with a net AFM order emerges in between the AFM₁, AFM₀, and ANq phases. This phase corresponds to the spin arrangement described in the third panel from the top in Figs. 2 and 4 and will be referred to as AFM₂.

For $\Delta = 0.8$ (lower rows in Figs. 5 and 6), as expected, the order of the magnetic and nematic transitions is reversed: The former precedes the latter as the temperature is lowered. Again, in line with the prediction based on the specific-heat behavior, only two possible phase transitions can be observed for all values of q . Furthermore, the broad shoulder appearing in the specific heat for $q = 4$ translates in a very gentle decay of the order parameter m_4 and a broad peak of the associated susceptibility χ_{m_4} .

Such a behavior is not typical for a phase transition, and therefore to better explore it we further perform a FSS analysis, based on the scaling relation (9), and study the associated correlation functions. To distinguish the AFM₀ phase with solely magnetic algebraic correlations from the AFM₁ phase with both magnetic and generalized nematic correlations, we study decays of the pair-correlation functions G_1 and G_q . In Fig. 7(a) we show for $q = 4$ the temperature dependencies of the corresponding critical exponents η_{m_1} (full symbols) and η_{m_4} (empty symbols), respectively, for different values of Δ . One can observe a sharp increase of η_{m_1} at the AFM₀-P phase transition but only a rather gentle increase of η_{m_4} spread over a wide temperature interval. Nevertheless, at least for larger values of Δ , it is apparent that the value of 1, corresponding to the exponential decay of the correlation function in the paramagnetic phase, is reached by

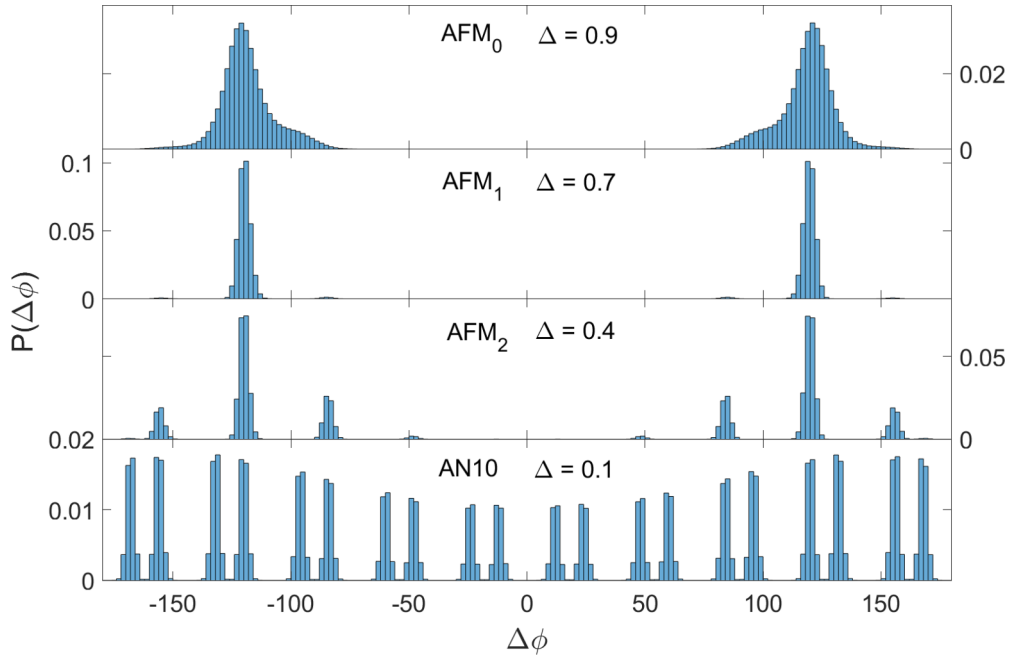


FIG. 4. Distributions of relative angles between neighboring spins in the observed phases for $q = 10$ at the fixed $T = 0.09$ and varying values of Δ , obtained from a single configuration snapshot with $L = 1536$.

η_{m_4} at temperatures lower than those corresponding to η_{m_1} . This finding tells us that the generalized nematic (AN4) correlations disappear before the magnetic (AFM)

ones, and thus it suggests the existence of separate AFM₁ and AFM₀ phases. However, the behavior of η_{m_4} is not typical for a standard phase transition, and

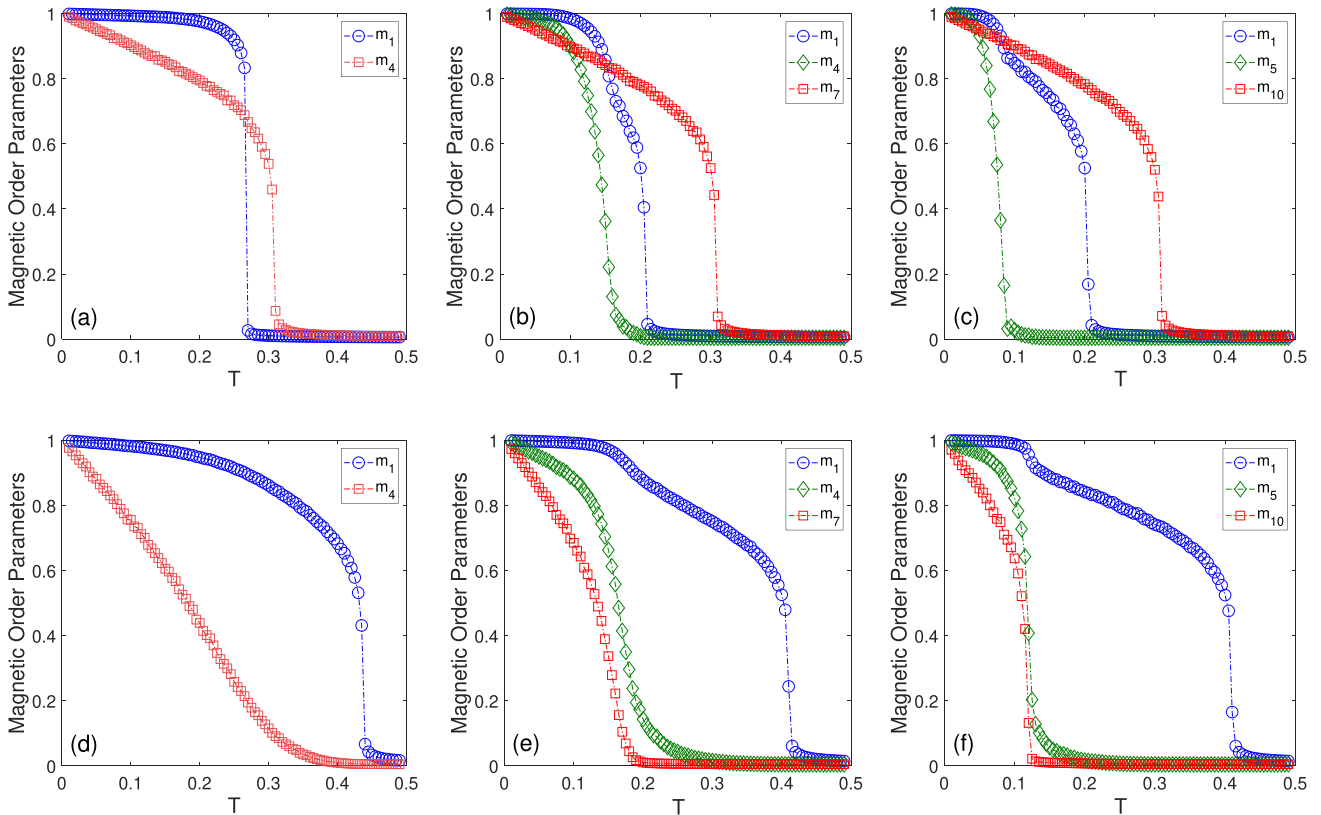


FIG. 5. Temperature dependencies of the standard and generalized magnetic order parameters for $q = 4$ (left column), $q = 7$ (middle column), and $q = 10$ (right column), corresponding to $\Delta = 0.4$ (upper row) and $\Delta = 0.8$ (lower row).

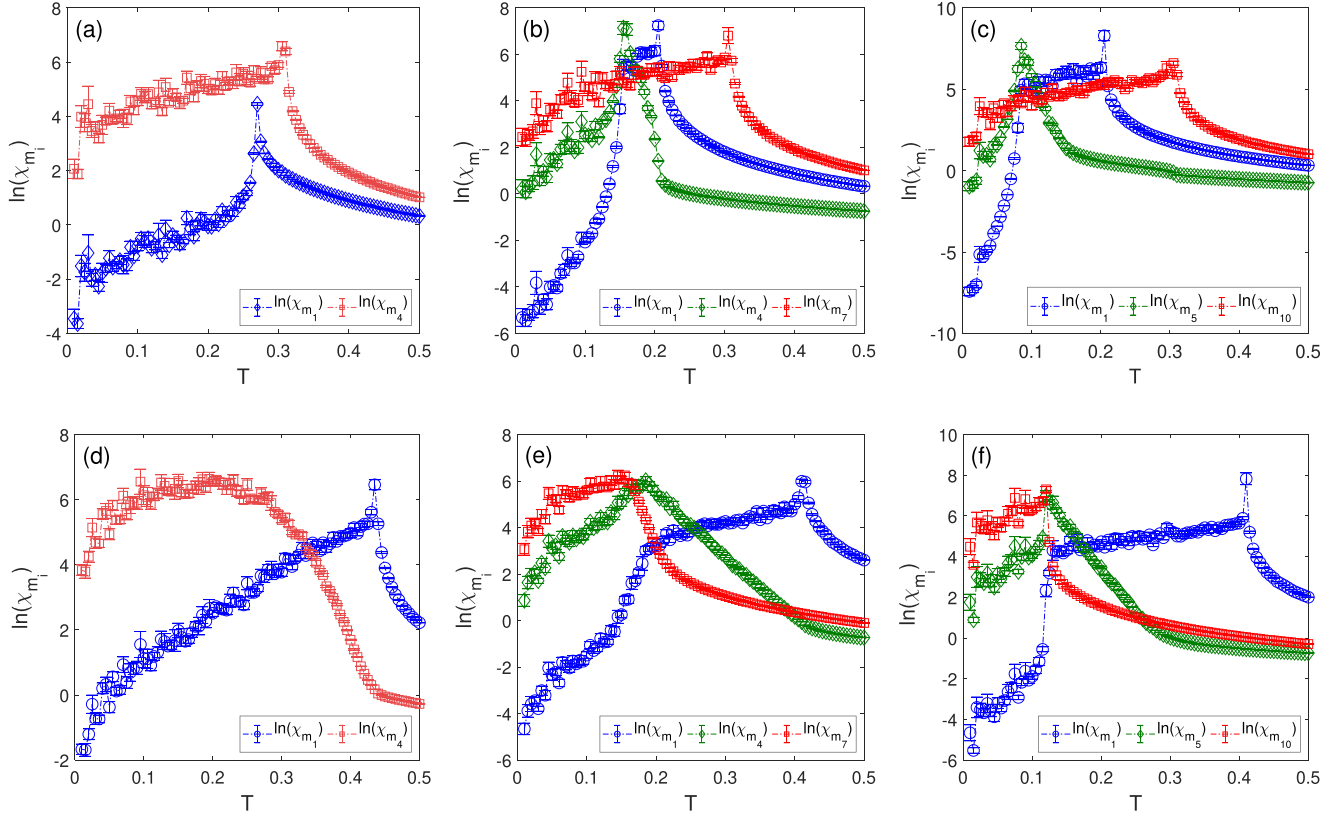


FIG. 6. Temperature dependencies of the standard and generalized magnetic susceptibilities for $q = 4$ (left column), $q = 7$ (middle column), and $q = 10$ (right column), corresponding to $\Delta = 0.4$ (upper row) and $\Delta = 0.8$ (lower row).

thus instead of a phase transition it might signal a crossover, which is not accompanied with a singular behavior.

In Fig. 7(b) we demonstrate the separation of the AFM₀ and AFM₁ phases with the increasing $q \geq 2$ (nondivisible by 3) for a fixed $\Delta = 0.8$. For $q = 2$ the transition to the paramagnetic phase clearly occurs at the same temperature, and

thus the two phases do not separate. The separation becomes apparent for $q = 4$, but the exponent η_{m_4} crosses to the value of 1 gradually over an extended interval of temperatures. With further increase of q the separation distance increases and the slope of η_{m_q} becomes sharper. The shape of η_{m_7} showing a relatively sharp increase is already much closer to the standard phase transition behavior. Nevertheless, the specific-heat

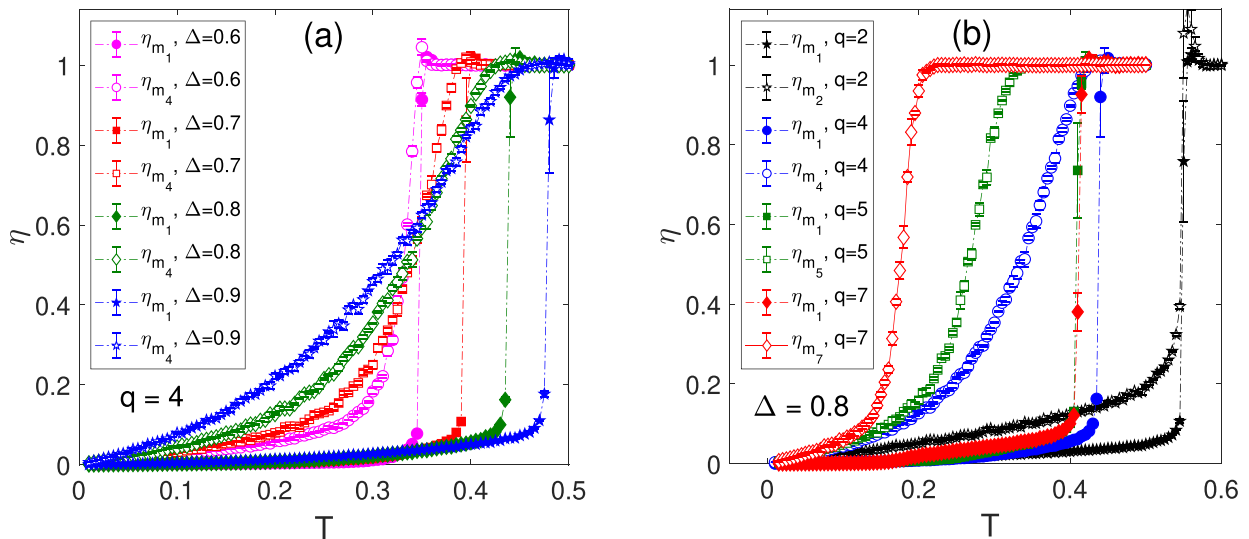


FIG. 7. Temperature dependencies of the critical exponents η_{m_1} (full symbols) and η_{m_q} (empty symbols), respectively, for (a) $q = 4$ and different values of Δ , and (b) $\Delta = 0.8$ and different values of q .

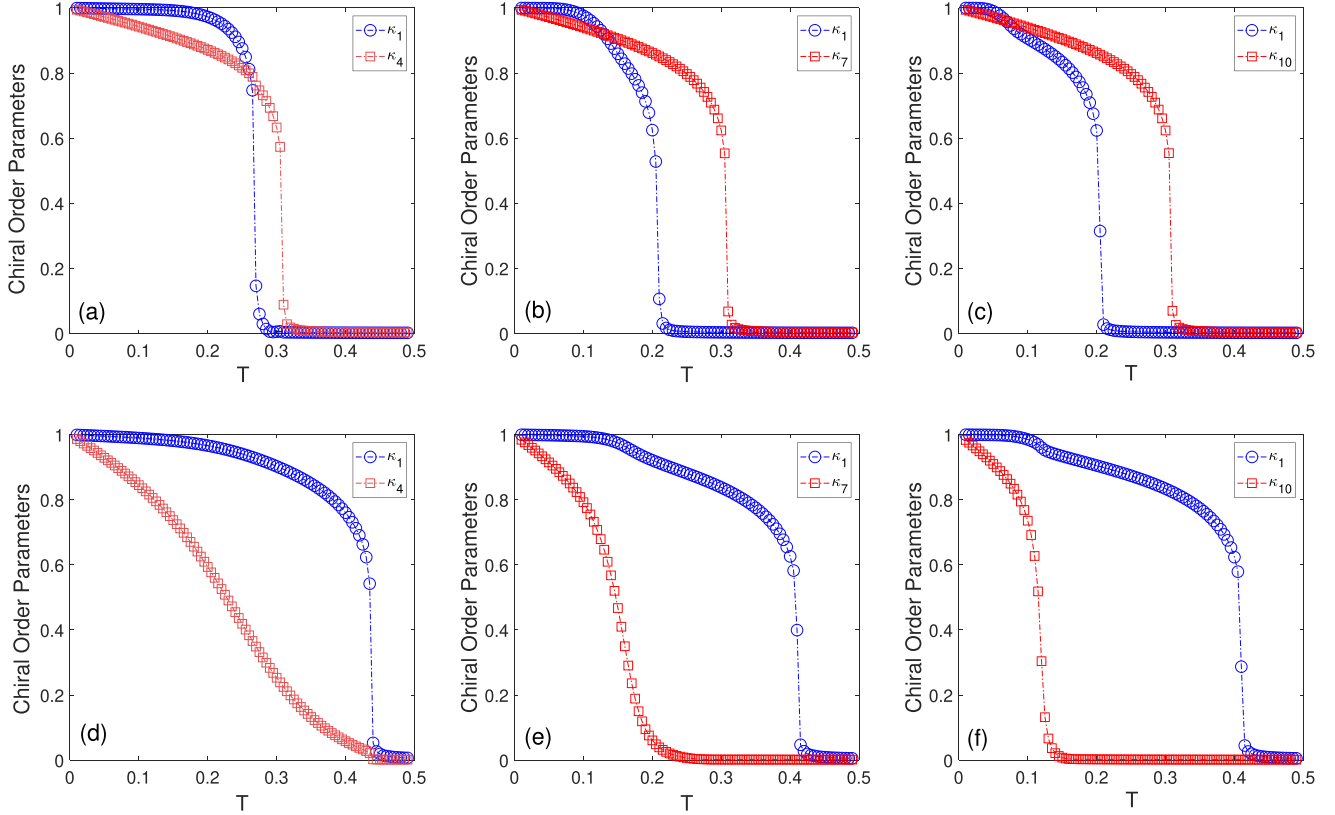


FIG. 8. Temperature dependencies of the standard and generalized chiral order parameters for $q = 4$ (left column), $q = 7$ (middle column), and $q = 10$ (right column), corresponding to $\Delta = 0.4$ (upper row) and $\Delta = 0.8$ (lower row).

curves presented in Fig. 1 would suggest instead that such a behavior, which would be reflected in a truly sharp peak, only occurs at still higher q . Our analysis confirms that for $\Delta = 0.8$ it happens starting from $q = 8$ (not shown). Nevertheless, as already indicated by the evolving shape of the specific-heat peaks, the behavior of η_{m_q} also depends on the value of Δ . Consequently, for sufficiently low $\Delta \approx 0.6$ it is possible to obtain the standard critical behavior at the AFM₀-AFM₁ phase transition with the sharp specific-heat peak and the sharp increase of η_{m_q} for the nematic parameter as low as $q = 5$. For $q = 4$ we were able to confirm by the correlation analysis the possibility of AFM₀ and AFM₁ phase separation, but it does not seem to occur via a standard phase transition for any value of Δ .

It is also interesting to notice that in the low-temperature AFM₁ phase, the magnetic correlation function decays extremely slowly. The associated critical exponent η_{m_1} (of the order of 10^{-4}) is about two orders of magnitude smaller than within the AFM₀ phase. This is also reflected in an even more dramatic drop of the magnetic susceptibility χ_{m_1} at the AFM₁-AFM₀ phase transition, as shown in Fig. 6. This behavior can be ascribed to the suppressed magnetic fluctuations in the AFM₁ phase, as demonstrated in Fig. 2.

Let us recall that in addition to the magnetic and nematic orderings, in the present frustrated model there are also (generalized) chirality orderings in the system. In Figs. 8 and 9 we present temperature dependencies of the standard and generalized staggered chiralities, κ_1 and κ_q , and the associated generalized chiral susceptibilities, χ_{κ_1} and χ_{κ_q} . We note that

in the previously studied $q = 3$ case, both of the chiral order parameters vanished only close to the transition to the paramagnetic phase. For $q > 3$, their behavior changes depending on q . In particular, for $0 < \Delta < 0.5$, κ_1 vanishes together with the magnetic order parameter m_1 at either the AFM₁-AN q or, for the values of q where the AFM₂ phase exists, at the AFM₂-AN q phase transition. Thus, only κ_q remains finite in the AN q phases. For $0.5 < \Delta < 1.0$, both chiralities remain finite in the intermediate AFM₀ phase for q up to 6. Note that in Fig. 8(d) the parameter κ_4 shows some decline below the transition to the paramagnetic phase; nevertheless, its value remains finite up to the temperature at which κ_1 vanishes. However, starting from $q = 7$, only κ_1 remains finite while κ_q copies the behavior of m_q and vanishes at the AFM₁-AFM₀ or AFM₂-AFM₀ transition. None of the chiral order parameters vanish at the AFM₁-AFM₂ transition, and all of the phases display at least one form of chiral ordering for all values of q .

The results are summarized in the phase diagrams shown in Fig. 10, which were constructed using the order parameter susceptibility peaks (squares) as well as the peaks in the specific-heat measurements (diamonds). The phase boundaries roughly estimated by these two methods show a rather good correspondence, except for the AFM₁-AFM₀ and AFM₁-AFM₂ phase boundaries, for which the specific-heat peaks predict, respectively, higher and lower transition temperatures than the corresponding susceptibilities peaks. We note that for $q = 4$ and 5 with larger Δ , the specific-heat curves do not provide a reliable estimate of the location of the AFM₁-AFM₀ phase boundary, as instead of sharp peaks

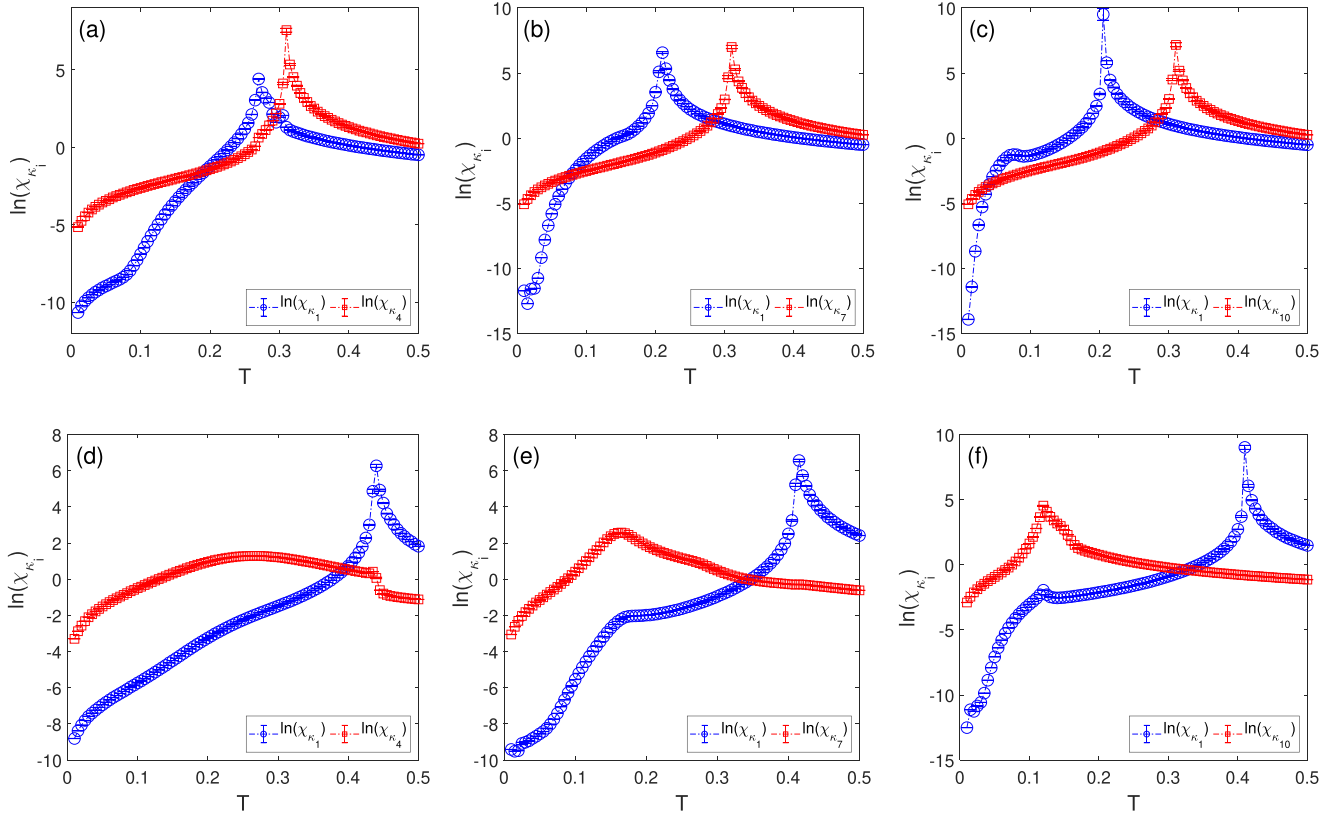


FIG. 9. Temperature dependencies of the standard and generalized chiral susceptibilities for $q = 4$ (left column), $q = 7$ (middle column), and $q = 10$ (right column), corresponding to $\Delta = 0.4$ (upper row) and $\Delta = 0.8$ (lower row).

they only show either broad shoulders ($q = 4$) or round and broad maxima ($q = 5$). Nevertheless, increasing the nematic parameter q from 4 to 5 does not seem to alter the system’s critical behavior, while $q = 6$ converts the low-temperature AFM₁ phase to the CAFM phase. The topology of the phase diagram for $q = 6$, as shown in Fig. 10(b), is similar to the $q = 3$ case from our previous work [23]. In fact, all the values of q divisible by 3 (up to $q = 15$ studied in this work) show the same magnetic phase diagram topology and no apparent deviations from the $q = 3$ case.

For $q = 7$ there is another change in the phase diagram topology. Namely, the AFM₁-AN_q phase transition line bifurcates, creating an additional AFM₂ phase. The region occupied by this new phase increases with q at the cost of the AFM₁ phase. The AFM₁-AFM₂ transition temperature appears to decrease with q for all values of Δ as q^{-2} , as shown in Fig. 11. There are no further changes in the phase diagram topology for q up to 14, the largest studied value of q nondivisible by 3.

IV. SUMMARY AND DISCUSSION

In this study, we have extended our previous work [23] on the critical behavior of the generalized XY model on a triangular lattice with AFM and generalized AN_q interactions for $q = 3$ by considering higher values of the generalized nematic parameter up to $q = 15$. As previously shown [31], the inclusion of the AN_q interaction for $q = 3$ and 6 changes the ground state from the usual AFM structure with $2\pi/3$

relative phase angles to a peculiar canted (CAFM) state. This change is caused by the ground-state competition between the AFM and AN_q interactions on the geometrically frustrated lattice and leads to phase diagrams containing three QLRO phases for all values of q divisible by 3 at least up to $q = 15$, the highest value studied in this work. Besides the CAFM phase with unsaturated values of the magnetic and generalized nematic order parameters down to zero temperatures, there are two intermediate-temperature phases with pure AFM and AN_q orderings.

In the case of q nondivisible by 3, the well-known phase diagram topology for $q = 2$ changes first at $q = 4$ and then again at $q = 7$. In particular, for $q = 4$ the AFM₀ phase with purely AFM correlations separates from the AFM₁ phase with the coexistent AFM and AN₄ correlations. In the AFM₁ phase, both the magnetic and generalized nematic order parameters reach saturated values at low temperatures, and the snapshots show typical AFM structure. Increasing the nematic parameter to $q = 7$ leads to the appearance of the AFM₂ phase in a part of the region previously occupied by the AFM₁ phase. This new phase still shows both the AFM and AN_q orderings; however, the typical AFM spin structure disappears. Instead, for each sublattice there are $\lceil q/2 \rceil$ possible spin orientations with different weights belonging to the same half-plane. The order parameter for the AFM₁-AFM₂ phase transition is $m_{\lceil q/2 \rceil}$.

All the observed phases display at least some kind of chiral LRO. In the low-temperature AFM₁ and AFM₂ phases, as well as the frustrated CAFM phase, both the standard κ_1

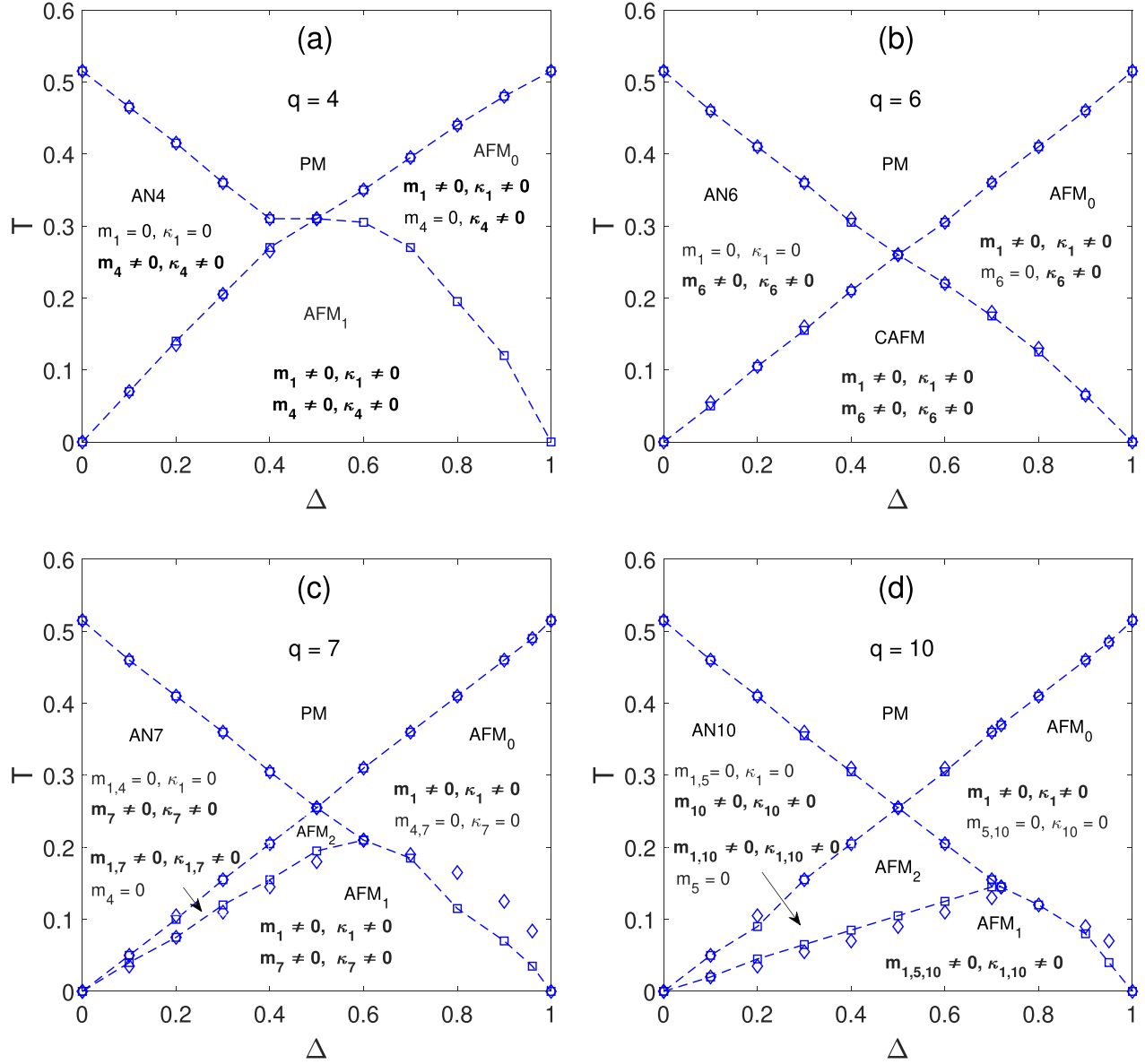


FIG. 10. Phase diagrams in the Δ - T parameter plane for representative values of $q = 4$ (a), 6 (b), 7 (c), and 10 (d). Diamond (square) symbols represent phase boundaries located from the peaks of the specific heat (generalized magnetic order susceptibility). In (a) the AFM $_0$ -AFM $_1$ phase boundary could not be estimated based on the specific heat due to the absence of a distinct peak for $q = 4$. The captions display the observed phases and the corresponding order parameters, with those taking finite values in the respective phases highlighted in bold.

and the generalized κ_q staggered chiralities remain finite. κ_1 vanishes at the transition to the AN q phase from the low-temperature phases for all q so that inside the AN q phases only κ_q remains finite. On the other hand, at the transition to the AFM $_0$ phase from the low-temperature phases, κ_q remains nonzero for q up to 6, while starting with $q = 7$ it drops to zero together with the nematic m_q order parameter at the AFM $_1$ -AFM $_0$ or AFM $_2$ -AFM $_0$ transition, and thus inside the AFM $_0$ phase only κ_1 remains finite.

It is interesting to compare the results for the present frustrated AFM-AN q models with those obtained for the related nonfrustrated models with FM-N q interactions on a square lattice [17–19]. It is worth noting that for $q = 2$ both systems display the same phase diagram topology (see, e.g., [13,14]). However, for $q > 2$, in the former case the ground-state com-

petition between the AFM and AN q interactions caused by the geometrical frustration arises for q divisible by 3, which is absent in the latter models, and leads to the formation of the CAFM phase. For q nondivisible by 3, there is no ground-state competition between the two interactions, and the results can be more easily compared. In the FM-N q models as q increases, a new QLRO phase appears for $q = 4$ at low temperatures due to the competition between the FM and N4 interactions, denoted in Ref. [19] as F $_1$ phase. Similar behavior was observed in the present AFM-AN4 model, accompanied by the emergence of the AFM $_1$ phase, albeit there might be a crossover rather than a standard phase transition to this phase. Further increase of the nematic parameter q to 5 results in another change in the phase diagram topology of the FM-N5 model, featuring the F $_2$ phase, while the topology of the

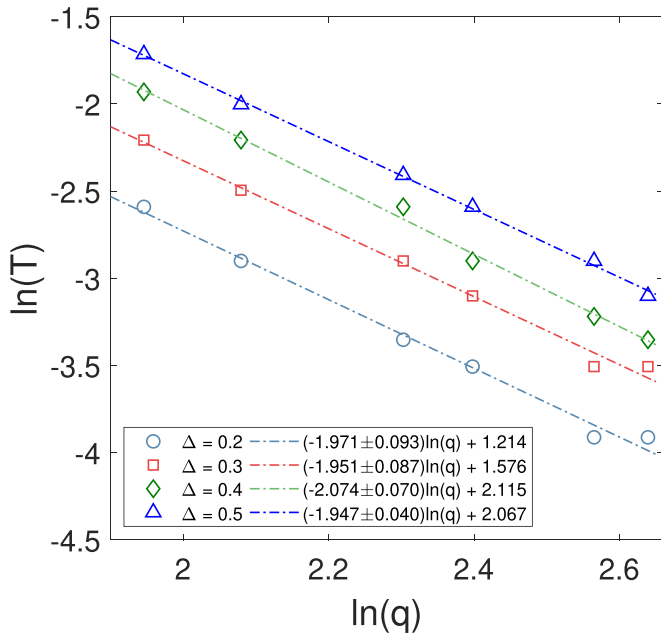


FIG. 11. Fits of the AFM₁-AFM₂ transition temperature dependence on the nematic parameter q , for various Δ .

the AFM-AN5 model seems to remain unchanged. Nevertheless, the AFM₂ phase, which might be viewed as a counterpart of the F₂ phase, appears in the present models for $q = 7$. Thus, except for the CAFM phase in the AFM-AN q models, which has no analog in the nonfrustrated FM-N q counterparts, the nature of the remaining phases in the two cases can be related. Namely, the respective types of orderings in the square-lattice FM-N q models can be observed on each of the three sublattices of the triangular-lattice AFM-AN q models. We think that because of the increased “stiffness” of the spin distributions in the latter models, due to the AFM constraints between spins belonging to different sublattices, a larger value of q is required for splitting the unimodal distribution in the AFM₁ phase to facilitate the emergence of the multimodal distribution in the AFM₂ phase. No further topology changes are observed in either model with the increasing q ; neverthe-

less, the area occupied by the F₂ and AFM₂ phases increases due to the power-law decrease of the F₂-F₁ and AFM₂-AFM₁ transition temperatures as q^{-2} .

Finally, the goal of the present study was the evolution of the phase diagram topology of the model with the increasing higher-order coupling, and we have not attempted to determine the character of all the identified phase transitions. As we found out when performing such an analysis for the $q = 3$ case [23], this task for the present frustrated systems in such a broad parameter space would require an enormous amount of additional simulations, and thus we leave it for future considerations. The main bottleneck is a huge autocorrelation time at the transition boundaries (including the crossover behavior), which hampers a reliable FSS analysis involving larger lattice sizes. Alternatively, one can suppress the autocorrelation time by opting for some more efficient nonlocal cluster algorithms. However, their implementation on GPU in the case of AFM systems composed of several sublattices is more complicated than in the case of FM systems. Moreover, compared to the local and thus naturally parallelized single spin-flip update simulations, for which the GPU implementation can lead to speedups of two to three orders of magnitude, the GPU implementation of the cluster algorithms is considerably more complicated even in the case of FM systems with much more modest expected speedups, especially close to criticality (up to about 30) [40]. Nevertheless, their implementation still leads to significant performance gains, and the interesting results obtained for their nonfrustrated counterparts [17–19], featuring phase transitions belonging to a variety of universality classes, as well as our findings pointing to the possibility of a crossover instead of a genuine phase transition along the AFM₀-AFM₁ and AFM₂-AFM₁ boundaries, would suggest that it is well worth trying.

ACKNOWLEDGMENTS

This work was supported by the Scientific Grant Agency of Ministry of Education of Slovak Republic (Grant No. 1/0531/19) and the Slovak Research and Development Agency (Contract No. APVV-18-0197). The authors would also like to thank the Joint Institute for Nuclear Research in Dubna, Russian Federation for the use of their Govorun Supercomputer.

- [1] N. D. Mermin and H. Wagner, *Phys. Rev. Lett.* **17**, 1133 (1966).
- [2] J. M. Kosterlitz and D. J. Thouless, *J. Phys. C* **6**, 1181 (1973).
- [3] J. M. Kosterlitz, *J. Phys. C* **7**, 1046 (1974).
- [4] E. Domany, M. Schick, and R. H. Swendsen, *Phys. Rev. Lett.* **52**, 1535 (1984).
- [5] D. H. Lee and G. Grinstein, *Phys. Rev. Lett.* **55**, 541 (1985).
- [6] S. E. Korshunov, *Pis'ma Zh. Eksp. Teor. Fiz.* **41**, 216 (1985) [*JETP Lett.* **41**, 263 (1985)].
- [7] T. J. Sluckin and T. Ziman, *J. Phys. France* **49**, 567 (1988).
- [8] D. B. Carpenter and J. T. Chalker, *J. Phys.: Condens. Matter* **1**, 4907 (1989).
- [9] S. Romano and V. Zagrebnoy, *Phys. Lett. A* **301**, 402 (2002).
- [10] L. X. Hayden, T. A. Kaplan, and S. D. Mahanti, *Phys. Rev. Lett.* **105**, 047203 (2010).
- [11] R. Hlubina, *Phys. Rev. B* **77**, 094503 (2008).
- [12] K. Qi, M. Qin, X. Jia, and J.-M. Liu, *J. Magn. Magn. Mater.* **340**, 127 (2013).
- [13] D. M. Hübscher and S. Wessel, *Phys. Rev. E* **87**, 062112 (2013).
- [14] J.-H. Park, S. Onoda, N. Nagaosa, and J. H. Han, *Phys. Rev. Lett.* **101**, 167202 (2008).
- [15] M. H. Qin, X. Chen, and J. M. Liu, *Phys. Rev. B* **80**, 224415 (2009).
- [16] M. Dian and R. Hlubina, *Phys. Rev. B* **84**, 224420 (2011).
- [17] F. C. Poderoso, J. J. Arenzon, and Y. Levin, *Phys. Rev. Lett.* **106**, 067202 (2011).
- [18] G. A. Canova, Y. Levin, and J. J. Arenzon, *Phys. Rev. E* **89**, 012126 (2014).

- [19] G. A. Canova, Y. Levin, and J. J. Arenzon, *Phys. Rev. E* **94**, 032140 (2016).
- [20] M. Žukovič and G. Kalagov, *Phys. Rev. E* **96**, 022158 (2017).
- [21] M. Žukovič and G. Kalagov, *Phys. Rev. E* **97**, 052101 (2018).
- [22] M. Žukovič, *Phys. Rev. E* **99**, 062112 (2019).
- [23] M. Lach and M. Žukovič, *Phys. Rev. E* **102**, 032113 (2020).
- [24] J. Pang, C. D. Muzny, and N. A. Clark, *Phys. Rev. Lett.* **69**, 2783 (1992).
- [25] L. Bonnes and S. Wessel, *Phys. Rev. B* **85**, 094513 (2012).
- [26] M. J. Bhaseen, S. Ejima, F. H. L. Essler, H. Fehske, M. Hohenadler, and B. D. Simons, *Phys. Rev. A* **85**, 033636 (2012).
- [27] A. Taroni, S. T. Bramwell, and P. C. W. Holdsworth, *J. Phys.: Condens. Matter* **20**, 275233 (2008).
- [28] G. M. Grason, *Europhys. Lett.* **83**, 58003 (2008).
- [29] A. B. Cairns, M. J. Cliffe, J. A. M. Paddison, D. Daisenberger, M. G. Tucker, F.-X. Coudert, and A. L. Goodwin, *Nat. Chem.* **8**, 442 (2016).
- [30] L. Clark and P. Lightfoot, *Nat. Chem.* **8**, 402 (2016).
- [31] M. Žukovič, *Phys. Rev. B* **94**, 014438 (2016).
- [32] M. Žukovič and D. T. Hristopulos, *Phys. Rev. E* **98**, 062135 (2018).
- [33] D. X. Nui, L. Tuan, N. D. Trung Kien, P. T. Huy, H. T. Dang, and D. X. Viet, *Phys. Rev. B* **98**, 144421 (2018).
- [34] S. Miyashita and H. Shiba, *J. Phys. Soc. Jpn.* **53**, 1145 (1984).
- [35] D. H. Lee, J. D. Joannopoulos, J. W. Negele, and D. P. Landau, *Phys. Rev. B* **33**, 450 (1986).
- [36] S. Lee and K.-C. Lee, *Phys. Rev. B* **57**, 8472 (1998).
- [37] S. E. Korshunov, *Phys. Rev. Lett.* **88**, 167007 (2002).
- [38] M. Hasenbusch, A. Pelissetto, and E. Vicari, *Phys. Rev. B* **72**, 184502 (2005).
- [39] T. Obuchi and H. Kawamura, *J. Phys. Soc. Jpn.* **81**, 054003 (2012).
- [40] M. Weigel, *Phys. Rev. E* **84**, 036709 (2011).